Optimized Chebyshev Fourier migration: A wide-angle dual-domain method for media with strong velocity contrasts

Jin-Hai Zhang[1], Wei-Min Wang[2], Shu-Qin Wang[3], and Zhen-Xing Yao[1]

ABSTRACT

A wide-angle propagator is essential when imaging complex media with strong lateral velocity contrasts in one-way wave-equation migration. We have developed a dual-domain one-way propagator using truncated Chebyshev polynomials and a globally optimized scheme. Our method increases the accuracy of the expanded square-root operator by adding two high-order terms to the traditional split-step Fourier propagator. First, we approximate the square-root operator using Taylor expansion around the reference background velocity. Then, we apply the first-kind Chebyshev polynomials to economize the results of the Taylor expansion. Finally, we optimize the constant coefficients using the globally optimized scheme, which are fixed and feasible for arbitrary velocity models. Theoretical analysis and numerical experiments have demonstrated that the method has very high accuracy and exceeds the unoptimized Fourier finite-difference propagator for the entire range of practical velocity contrasts. The accurate propagation angle of the method is always about 60° under the relative error of 1% for complex media with weak, moderate, and even strong lateral velocity contrasts. The method allows us to handle wide-angle propagations and strong lateral velocity contrast simultaneously by using Fourier transform alone. Only four 2D Fourier transforms are required for each step of 3D wavefield extrapolation, and the computing cost is similar to that of the Fourier finite-difference method. Compared with the finite-difference method, our method has no two-way splitting error (i.e., azimuthal-anisotropy error) for 3D cases and almost no numerical dispersion for coarse grids. In addition, it has strong potential to be accelerated when an enhanced fast Fourier transform algorithm emerges.

INTRODUCTION

The one-way wave equation, also known as the paraxial wave equation, is widely applied to the propagation of acoustic waves in underwater acoustics and geophysics. The one-way wave-equation method divides the 3D velocity model into a sequence of 2D thin slabs along the preferred direction (e.g., the depth direction), and the wavefields in the current slab are generated iteratively from the wavefields in the previous slab. Although the reflected waves along the preferred direction are neglected (Claerbout, 1985; Wu, 1994; Xie and Wu, 2001), the forward diffraction and refraction are handled well (Wu, 1994). Compared with the two-way wave-equation method (Baysal et al., 1983; Loewenthal and Mufti, 1983), the one-way wave equation method is much more computationally efficient and has fewer memory demands because it uses the spatial iterative algorithm rather than a temporal iterative algorithm. These features of the one-way wave-equation method are important for solving large-scale 3D problems.

The finite-difference method (Claerbout, 1985) is a popular solution of the one-way wave equation. It can handle strong velocity variations. However, it has significant numerical dispersion for coarse grids and high-frequency components, which are harmful to high-resolution imaging of steep dips. In addition, the commonly used two-way splitting technique (i.e., alternating-direction-implicit scheme) for 3D extension leads to large phase errors (two-way splitting errors), especially for steep dips in diagonal directions (Brown, 1983; Wang, 2001); consequently, additional efforts are required to compensate for the two-way splitting error (e.g., Li, 1991; Wang, 2001; J. Zhang et al., 2008).

Another solution of the one-way wave equation is the Fourier

method (Gazdag, 1978; Kosloff and Baysal, 1983; Stoffa et al., 1990), also termed the dual-domain method, using Fourier transforms to perform wavefield extrapolation. Compared with the finite-difference method, the Fourier method is immune to numerical dispersions and two-way splitting errors; in addition, it is more efficient because of using fast Fourier transforms (FFTs). However, low-order Fourier methods (Stoffa et al., 1990; Wu, 1994) are limited to small-angle propagations and weak lateral velocity variations; thus, they have difficulties handling wide-angle propagations and strong lateral velocity contrast simultaneously (Cheng et al., 1996; Huang and Fehler, 1998).

Various schemes have been proposed to improve the accuracy of the Fourier method. One popular way is to approximate the one-way wave equation using high-order expansion (Huang et al., 1999a, 1999b; de Hoop et al., 2000; Huang and Fehler, 2000b; Fu, 2005). Another popular way is to optimize the constant coefficients of the Fourier propagator (Liu and Zhang, 2006; Zhang and Liu, 2007). There are also two distinct, high-order Fourier methods: the phase-shift plus interpolation (PSPI) method (Gazdag and Sguazzero, 1984) and the optimum separable approximation (Chen and Liu, 2004). These two methods can image steep dips in complex media with strong velocity contrasts, but the former requires too many Fourier transforms compared with the other high-order Fourier methods, and the latter is costly during singular value decomposition. Besides these pure Fourier methods, the hybrid Fourier finite-difference method uses a finite-difference scheme to perform the high-order corrections after the low-order Fourier method (Ristow and Rühl, 1994; Biondi, 2002).

Under the same condition of time consumption, the maximum accurate propagation angle of current Fourier methods is much lower than that of the optimized Fourier finite-difference method (Huang and Fehler, 2000a; Zhu et al., 2008) in the presence of complex media with strong lateral velocity contrasts. For example, the globally optimized Fourier finite-difference method based on multiparameters has an accurate propagation angle of about 75° for arbitrary velocity contrasts (Zhu et al., 2008). In contrast, the generalized-screen method (de Hoop et al., 2000; Le Rousseau and de Hoop, 2001) can achieve the same wide-angle accuracy only for weak velocity contrasts (J. Zhang et al., 2009b), and the optimized generalized-screen method (Liu and Zhang, 2006) can achieve the same wide-angle accuracy only for weak and moderate velocity contrasts. The low accuracy of the Fourier propagator in the presence of strong velocity contrasts and wide-angle propagation is basically associated with low-accuracy approximations, such as Taylor expansion or power series expansion. These low-accuracy approximations usually have low convergence, so we would have little benefit even with many higher-order terms added. Therefore, we should use a better approximation approach to significantly enhance the performance of the Fourier propagator.

Chebyshev polynomials are very important in the field of numerical approximation. As long as we are approximating a smooth function, the Chebyshev polynomials minimize the largest deviation from the original function among the polynomials of the same order (Mason and Handscomb, 2003). As a result, the Chebyshev polynomials converge faster than the Taylor expansion (or power series expansion) for the same function in terms of the maximum error. The Chebyshev polynomials have been introduced to improve the wide-angle accuracy of the finite-difference propagator (Kelamis, 1988) and the Fourier finite-difference method (Sen and Anandakrishnan, 2003). Under the same condition of time consumption, the Cheby-

shev polynomials provide a much more flexible finite-difference scheme to approach the square-root operator compared with the commonly used Taylor and Padé expansions (G. Zhang et al., 1988).

In this paper, we use the Chebyshev polynomials to improve the wide-angle accuracy of the high-order Fourier propagator, especially for complex media with strong velocity contrasts. The proposed scheme first approximates the square-root operator using Taylor expansion around the reference slowness up to the third order. Then the first-kind Chebyshev polynomials are used to rearrange the partial derivative coefficients. Finally, the constant coefficients are optimized using the globally optimized scheme (Huang and Fehler, 2000a; Zhu et al., 2008). Our proposed scheme is similar to that of Sen and Anandakrishnan (2003), but we perform high-order corrections by the Fourier method rather than the finite-difference method. We illustrate the method using theoretical analysis, impulse responses, and synthetic data of the SEG/EAGE salt model.

METHODOLOGY

One-way Fourier propagators using truncated Chebyshev polynomials

The vertical wavenumber for 2D one-way wavefield extrapolator reads

$$k_z = \sqrt{\omega^2 s^2 - k_x^2}, \qquad (1)$$

where $s = 1/V(x)$ is the slowness slice at the depth level of z, ω is the angular frequency, and k_x is the horizontal wavenumber. Equation 1 is also called the dispersion relation; it handles the phase changes of wavefield propagations. Usually, a constant slowness $c = V_0$, also called reference slowness, can be selected as the background of the laterally varying slowness s (Stoffa et al., 1990; Wu, 1994). Applying the Nth-order Taylor expansion to the vertical wavenumber k_z around the maximum reference slowness $c = 1/\min[V(x)]$ yields

$$k_z \approx \sqrt{\omega^2 c^2 - k_x^2} + \sum_{n=1}^{N} \frac{1}{n!} \left. \frac{\partial^n k_z}{\partial s^n} \right|_c \Delta s^n, \qquad (2)$$

where $\Delta s = s - c = c(p-1)$ is the slowness perturbation, $p = s/c$ is the refraction index, and

$$\left. \frac{\partial k_z}{\partial s} \right|_c = \omega^2 c (\omega^2 c^2 - k_x^2)^{-1/2},$$

$$\left. \frac{\partial^2 k_z}{\partial s^2} \right|_c = -\omega^2 k_x^2 (\omega^2 c^2 - k_x^2)^{-3/2},$$

$$\left. \frac{\partial^3 k_z}{\partial s^3} \right|_c = 3\omega^4 k_x^2 c (\omega^2 c^2 - k_x^2)^{-5/2},$$

$$\left. \frac{\partial^4 k_z}{\partial s^4} \right|_c = -3\omega^4 k_x^2 (4\omega^2 c^2 + k_x^2)(\omega^2 c^2 - k_x^2)^{-7/2}. \quad (3)$$

Using the truncated Chebyshev polynomials to the Taylor expansion of the vertical wavenumber (equation 2), we obtain the general form of the Nth-order propagator (see Appendices A–C for details):

$$k_z \approx k_z^0 + \omega \Delta s + k_z^C, \qquad (4)$$

where $k_z^0 = \sqrt{\omega^2 c^2 - k_x^2}$ is the vertical wavenumber in reference media and where

$$k_z^C = \omega \sum_{n=1}^{N} \left(\frac{k_x^2}{\omega^2 c^2} \right)^n b_n(\Delta s, P_0) \tag{5}$$

is the sum of the first N terms associated with the wavenumber and spatial variables. In equation 5, the wavenumber variables k_x^2 and spatial variables $s(x)$ are separable for each order. When $N = 2$, b_n are (see Appendix B for details)

$$b_1 = \frac{47\Delta s}{64} - \frac{1}{2c}\Delta s^2 + P_0,$$

$$b_2 = \frac{3\Delta s}{8} - \frac{3}{4c}\Delta s^2 + \frac{5}{2}P_0, \tag{6}$$

with

$$P_0 = \frac{P^3}{64c^2} - \frac{9P^2}{32c^2}\Delta s + \frac{3P}{4c^2}\Delta s^2$$

and $P \equiv c[\min(p) - 1]$.

The solutions of the one-way wave equation for lateral velocity variations decompose into the following cascade equations:

$$u'(x,z + \Delta z;\omega) = F^-\{\exp(ik_z^0\Delta z)F^+[u(x,z;\omega)]\}, \tag{7}$$

$$u''(x,z + \Delta z;\omega) = \exp(i\omega\Delta s\Delta z)u'(x,z + \Delta z;\omega), \tag{8}$$

$$u(x,z + \Delta z;\omega) = \exp(ik_z^C\Delta z)u''(x,z + \Delta z;\omega), \tag{9}$$

where Δz is the depth step of the horizontal thin slab and where F^+ and F^- denote forward and inverse Fourier transforms, respectively. Equation 7 performs the phase shift in the reference slowness c (Gazdag, 1978), and equation 8 performs the time-shift corrections associated with the slowness perturbations Δs. These two equations compose the well-known split-step Fourier method (Stoffa et al., 1990) or phase-screen method (Wu, 1994), which is accurate only for small-angle propagations under weak lateral velocity variations.

Equation 9 performs the high-order corrections after the phase-shift and time-shift terms. We want to construct these high-order corrections using the Fourier scheme rather than the finite-difference scheme to handle wide-angle propagations under moderate and even strong lateral velocity variations. However, the spatial variables Δs are not explicitly separated from the wavenumber variables k_x^2 because they are coupled as the exponent of a complex exponential function (see equation 9). Another Taylor expansion (i.e., $e^{ix} \approx 1 + ix$) is required for the exponential function in equation 9 to separate the spatial and wavenumber variables completely (de Hoop et al., 2000). Thus, the high-order corrections are further approximated as

$$u(x,z + \Delta z;\omega) \approx (1 + ik_z^C\Delta z)u''(x,z + \Delta z;\omega). \tag{10}$$

The phase-screen method (i.e., equations 7 and 8) can handle the phase-shift correction in the homogeneous background velocity and the time-shift correction in the depth direction (i.e., the preferred direction). The high-order terms (i.e., equation 9) only handle the corrections of wide-angle propagation away from the depth direction. Thus, the exponent $ik_z^C\Delta z$ is very small for small-angle propagation or weak velocity contrast, and the Taylor expansion used in equation 10 is reasonable. For wide-angle propagation in media with strong lateral velocity contrasts, however, this expansion would introduce

relatively large phase error. De Hoop et al. (2000) suggest a normalization operator $\mathcal{N}$ to reduce the phase error caused by the Taylor expansion used in equation 10, which reads

$$\mathcal{N}(1 + p + iq) = \exp(iq)\left| 1 + \frac{p}{1 + iq} \right|^{-1}\left(1 + \frac{p}{1 + iq} \right), \tag{11}$$

where p and q denote the real and imaginary parts of a complex number, respectively.

In implementation, the variables associated with $b_n(\Delta s, P_0)$ are handled in the spatial domain and the variables associated with $k_x^2/(\omega^2 c^2)$ are handled in the wavenumber domain, where FFTs are used to shuttle the wavefields between spatial and wavenumber domains. A detailed wavefield extrapolation procedure for high-order corrections is

$$u(x,z + \Delta z) = u''(x,z + \Delta z;\omega) + F^-\left\{ i\omega\Delta z \sum_{n=1}^{N} \left(\frac{k_x^2}{\omega^2 c^2} \right)^n \right.$$
$$\left. \times F^+[b_n u''(x,z + \Delta z;\omega)] \right\}. \tag{12}$$

Global optimization by simulated annealing

In addition to Taylor expansion for variable separations, several approximations are caused by power-series expansion of fractional-exponential functions $\partial^n k_z/\partial s^n|_c$ (see equations C-4 and D-8 for details). To reduce the error caused by these approximations yet retain the orders and computing cost, we should optimize the constant coefficients in b_n. However, the value of the parameter P_0 in b_n is associated with maximum slowness and minimum slowness in a horizontal velocity slice. It is possible to apply a locally optimized scheme that produces optimized coefficients for each lateral velocity variation, but a large table of optimized coefficients is required.

Huang and Fehler (2000a) propose a globally optimized scheme whereby optimized coefficients are associated only with the maximum velocity contrast in the whole model. This globally optimized scheme makes it possible to produce a group of fixed optimized coefficients for arbitrary models in advance. We approximate the variable $P_1 = P_0/\Delta s$ to be associated with refraction index p but independent from variable $P \equiv c[\min(p) - 1]$. The constant coefficient of variable $P_1 = P_0/\Delta s$ thus is over $[-1,1]$ and hence can be determined by the globally optimized scheme.

When $N = 2$, the spatial variables b_n in equation 6 can be rewritten in another form:

$$b_1 = \frac{\Delta s}{2}\left(\frac{79}{32} - p + 2P_1 \right),$$

$$b_2 = \frac{\Delta s}{8}(9 - 6p + 20P_1). \tag{13}$$

For the convenience of optimization and practical applications, we rewrite the spatial-associated terms of the propagator shown in equation 13 as

$$b_1 = f_1\Delta s\left(\frac{79}{32} - p + 2\frac{P_1}{p^2} \right),$$

$$b_2 = f_2 \Delta s \left(9 - 6p + 20 \frac{P_1}{p^2} \right), \tag{14}$$

where $f_1, f_2,$ and P_1 are constant coefficients that are ready to be optimized over $[0,1]$.

The percentage velocity contrast is defined as $(V - V_0)/V \times 100\% = (1 - p) \times 100\%$. A small velocity contrast denotes weak lateral velocity variations, and a big one denotes strong lateral velocity variations. For example, it equals 0% for laterally homogeneous media and equals 100% for extremely strong lateral velocity variations. As in the globally optimized scheme (Huang and Fehler, 2000a), we divide the practical range of $[1, 1/p_{min}]$ with a uniform interval of 0.1, where $p_{min} = \min[s/c]$. We can rewrite the vertical wavenumber of the second-order optimized Chebyshev Fourier propagator in terms of the propagation angle θ as

$$k_z \approx k_z^0 + \omega \Delta s + k_z^C = \omega s R, \tag{15}$$

where

$$R = \frac{1}{p}\sqrt{1 - p^2 \sin^2 \theta} + \left(1 - \frac{1}{p} \right) + f_1 p^2 \sin^2 \theta \left(1 - \frac{1}{p} \right) \left(\frac{79}{32} \right.$$
$$\left. - p + 2\frac{P_1}{p^2} \right) + f_2 p^4 \sin^4 \theta \left(1 - \frac{1}{p} \right) \left(9 - 6p + 20\frac{P_1}{p^2} \right). \tag{16}$$

We use simulated annealing (Kirkpatrick et al., 1983) to minimize the percentage relative error of the approximated vertical wavenumber k_z according to the object function

$$E(\theta, p) = \left| \frac{k_z - \bar{k}_z}{\bar{k}_z} \right| \times 100\%$$
$$= \left| \frac{R - \cos \theta}{\cos \theta} \right| \times 100\% \le 1\%, \tag{17}$$

where $\bar{k}_z = \omega s \cos \theta$ denotes the theoretical vertical wavenumber in terms of the propagation angle θ and where k_z denotes the approximated vertical wavenumber in terms of the propagation angle θ, with $k_x^2 = \omega^2 s^2 \sin^2 \theta$.

Over the range of $p \in [1/3, 1]$ under the relative error of 1%, the optimized coefficients obtained are $f_1 = 0.0989173$, $f_2 = 0.0736847$, and $P_1 = 0.6728358$. These parameters are available to arbitrary velocity contrasts for all known practical models, including salt-related models. In addition, these optimized coefficients can be applied to 3D cases with no difficulty, although they are based on the optimization of a 2D operator. In implementation, we need to replace the vertical wavenumber k_x^2 with $k_x^2 + k_y^2$ and replace 1D Fourier transforms $F^\pm$ with 2D ones.

The proposed optimized Chebyshev Fourier method is similar to the generalized-screen method (de Hoop et al., 2000) in the aspect that they can use FFTs to perform wavefield extrapolation. Thus, our method can speed up one order of magnitude when using the newly developed computing scheme of Fourier depth migration based on graphics processing units (J. Zhang et al., 2009a). The basic difference between our method and the generalized-screen method lies in the detailed forms of spatial and wavenumber variables, which leads to the discrepancy between stability and accuracy. The generalized-screen method has singularity problems at high wavenumbers because the phase-shift operator for reference slowness emerges in the denominator of the high-order corrections. In contrast, there is no singularity in the high-order corrections of our optimized Chebyshev Fourier method.

Phase-error analysis

We discretize the propagation angle θ in the object function (equation 17) over $[0°, 90°]$ with an interval of 0.1°. For a given refraction index $p = s/c$, we can plot the corresponding curve of the optimized Chebyshev Fourier method in terms of relative errors versus dip angles. For each independent refraction index p over $[1/3, 1]$ with an interval of 0.01, if we remember the dip angle that begins to exceed the threshold 1%, we can plot the curve of maximum accurate angle versus velocity contrasts. These two kinds of curves are usually used to evaluate the performance of a propagator (Li, 1991; Huang and Fehler, 2000a; J. Zhang et al., 2009b).

Figure 1 shows relative errors versus dip angle for the split-step Fourier (SSF), Fourier finite-difference (FFD), globally optimized Fourier finite-difference (GOFFD), and optimized Chebyshev Fourier (OCF) methods. The maximum dip angle of the OCF method is generally beyond that of the unoptimized FFD method but below that of the GOFFD method. When $V/V_0 = c/s = 1/p$ varies from 1.5 to 3.0 with an interval of 0.5, the relative-error curves of the SSF and unoptimized FFD methods grow gradually with the increasing dip angle and exceed 1% at a relatively small dip angle. In contrast, the relative-error curves of the GOFFD and OCF methods try to vibrate within the relative phase error of 1% and exceed 1% at a much larger dip angle.

Figure 2 shows the maximum accurate angle of various methods for a practical range of lateral velocity contrasts. For each method, the relative phase error is not bigger than 1% under the curve but begins to exceed 1% above the curve. Obviously, the SSF method has the lowest accuracy among all methods listed when the maximum slowness is used. The generalized-screen methods have significant improvement for weak lateral velocity contrast but rapidly degener-
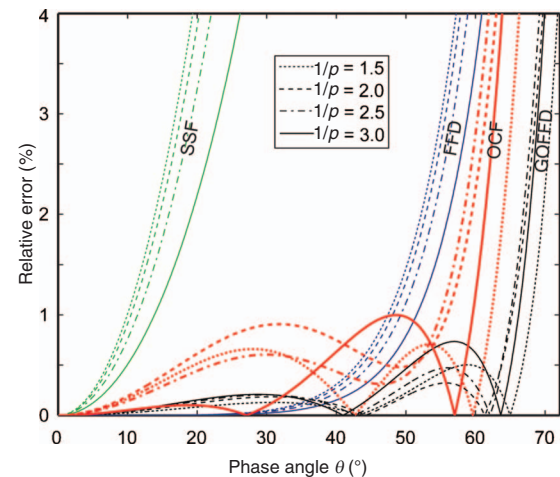

Figure 1. Comparison of percentage relative errors versus dip angles when $V/V_0 = 1/p$ varies from 1.5 to 3.0 with an interval of 0.5. The green lines denote the split-step Fourier method (SSF); the red bold lines denote the proposed optimized Chebyshev Fourier method (OCF); the blue lines denote the Fourier finite-difference method (FFD); and the black lines denote the globally optimized Fourier finite-difference method (GOFFD).

ate into the SSF method when velocity contrasts increase. The unoptimized FFD method is an improvement over the SSF method of about 40° for the whole range of velocity contrasts listed, and the GOFFD method has further improvement of about 20°. The OCF method is accurate around 60° for the whole range of lateral velocity contrasts listed. This accuracy is much higher than the unoptimized FFD method at about 10°.

NUMERICAL EXAMPLES

Migration impulse responses

We demonstrate the performance of the OCF method using impulse responses. A 3D homogeneous medium is defined on a $256 \times 256 \times 128$ grid system with a grid spacing of 10 m (20 m for coarse grids). The real velocity is $V = 4500$ m/s. The input trace is located at the center of the upper model boundary. The dominant frequency of the Ricker wavelet is 30 Hz. The time delay of the wavelet is 250 ms for a grid spacing of 10 m (500 ms for a grid spacing of 20 m) with a sampling interval of 2 ms. The frequency range calculated in the migration is $0 \sim 117$ Hz with 120 components. The attenuation band of the tapered function for the absorbing boundary condition has 15 samples on each side of the 2D wavefield. No wavenumber filter is used during the wavefield extrapolation.

Figure 3 shows the vertical slices from 3D migration impulse responses. Each view shows the superposition of the vertical slices obtained by the second-order generalized-screen (GSP2) method and the OCF method. The reference velocities used for the left and right parts of Figure 3a are $V_0 = 1500$ m/s [i.e., strong velocity contrast $(V - V_0)/V = 66.7\%)$] and 2250 m/s [i.e., large velocity contrast $(V - V_0)/V = 50\%$], respectively. The reference velocities used for the left and right parts of Figure 3b are $V_0 = 3000$ m/s [i.e., moderate velocity contrast $(V - V_0)/V = 33.3\%$] and 3750 m/s [i.e., weak velocity contrast $(V - V_0)/V = 16.7\%$], respectively. Obvi-

ously, the impulse responses obtained by the GSP2 method deviate significantly from the exact position (indicated by the dashed semicircle) even for small dip angle when the velocity contrast is greater than 50%. In contrast, the impulse responses of the proposed method are always close to the exact positions up to 60° when the velocity contrast is weak, moderate, and even strong.

Figure 4 shows the depth slices of 3D migration impulse responses at a dip angle of 60° away from the depth direction. There are four equivalent parts: the upper-left quadrant is for $V_0 = 1500$ m/s, the lower-left quadrant is for $V_0 = 2250$ m/s, the lower-right quadrant is for $V_0 = 3000$ m/s, and the upper-right quadrant is for $V_0 = 3750$ m/s. Each part shows the superposition of the depth slices obtained by the GPS2 and OCF methods. The impulse responses of the GPS2 method significantly deviate from the exact position (indicated by the dashed circle) except for the weak velocity contrast $(V - V_0)/V = 16.7\%$. In contrast, the impulse responses of the OCF method are always close to the exact positions (indicated by the dashed circle) for all velocity contrasts listed, whether weak, moderate, or strong.

The FFD method (Ristow and Rühl, 1994; Biondi, 2002) is well known in imaging complex media with strong velocity contrasts. It is selected as a reference to evaluate the OCF method. The two-way splitting scheme (Brown, 1983) is used without compensation for the two-way splitting error (Li, 1991; Wang, 2001; J. Zhang et al., 2008). Figure 5 shows the vertical slices obtained by the FFD and OCF methods. Obviously, the maximum accurate dip angle of the OCF method is comparable to that of the FFD method when using a grid interval of 10 m, as shown in Figure 5a. In Figure 5b, however,
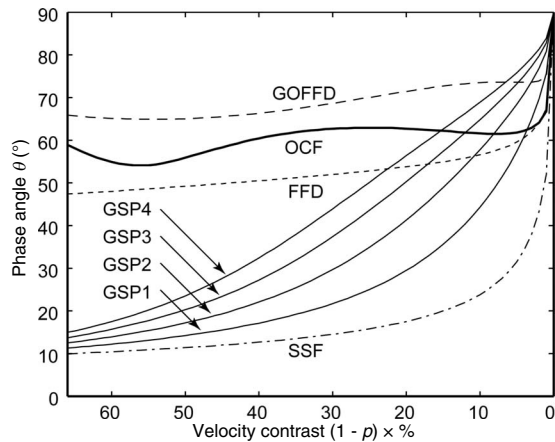

Figure 2. Comparison of maximum dip angles versus the lateral velocity contrasts for various methods under a relative error of 1%. The velocity contrast is defined as $(V - V_0)/V \times 100\% = (1 - p) \times 100\%$. A small velocity contrast denotes weak lateral velocity variations; a large one denotes strong lateral velocity variations. For each method, above the line, the error is larger than the chosen relative error; below, it is smaller. The dashed-dotted line denotes the SSF method, the short dashed line denotes the FFD method, the long dashed line denotes the GOFFD method, the bold solid line denotes the proposed OCF method, and the solid lines indicated by arrows denote the first four orders of the generalized-screen method, i.e., GSP1, GSP2, GSP3, and GSP4, respectively.
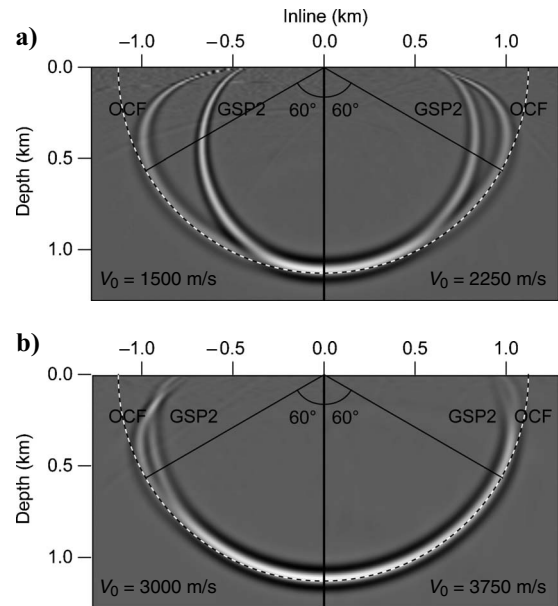

Figure 3. Superposition of vertical slices obtained by 3D impulse responses. Each panel consists of two equivalent parts, and different parts use a different reference velocity. Each part shows the superposition of the vertical slices obtained by the GSP2 method (inner bowls) and the OCF method (outer bowls). The dashed semicircle indicates the ideal position. The real velocity of a homogeneous medium is $V = 1/s = 4500$ m/s, and the reference velocity used is (a) $V_0 = 1/c = 1500$ m/s (left side) and 2250 m/s (right side), and (b) 3000 m/s (left side) and 3750 m/s (right side). The grid interval used in migration is 10 m. The dominant frequency of the Ricker wavelet is 30 Hz.

significant numerical dispersion emerges at the dip-angle range of 40°~90° for the FFD method when using a relatively coarse grid interval of 20 m. In contrast, the OCF method achieves very high ac-

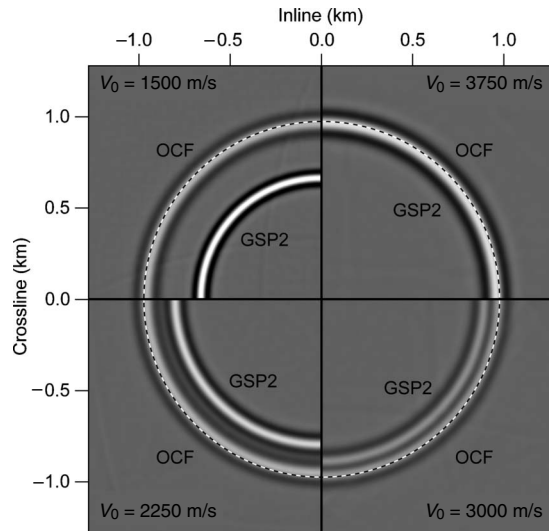curate dip angle as does the FFD method, but there is no numerical dispersion for a small grid of 10 m or for a relatively coarse grid of 20 m.

Figure 6 shows the depth slices of the two-way splitting FFD method and the OCF method. For the strong velocity contrast of ($V - V_0)/V = 66.7\%$ (often associated with salt models), the GOFFD and the OCF methods obtain high accuracy for wide angles, but the FFD method has significant numerical dispersions for a relatively coarse grid and significant splitting errors, especially in diagonal directions (see the left parts). The splitting error can be reduced using additional correction techniques (e.g., Li, 1991; Wang, 2001; J. Zhang et al., 2008), but numerical dispersions are difficult to reduce. In contrast, the results obtained by the OCF method are very clear and accurate, with no numerical dispersion or splitting error.

These three methods — GSP2, OCF, and FFD — have similar computing costs under the same hardware and software conditions, and each runs about 680 s. A hybrid radix FFT, one of the fastest CPU-based algorithms, is used in our code.

Migration for SEG/EAGE salt model

To verify accuracy and efficiency of the OCF method on imaging 3D complex structures, we test on zero-offset records (Ober et al., 1997) of the SEG/EAGE salt model (Aminzadeh et al., 1996). We extract every other grid point along inline and crossline directions from the original data. That is, the 3D grid system used here is 250 $\times 250 \times 210$ with a spacing of 40 m along the transverse direction and 20 m along the depth direction. The frequency range calculated in the migration is $0 \sim 30$ Hz with 120 components. The attenuation

Figure 4. Superposition of depth slices obtained by 3D impulse responses. This picture consists of four equivalent parts, and different parts use different reference velocities. Each part shows the superposition of the depth slices obtained by the GSP2 method (inner arches) and the OCF method (outer arches). The dashed circle indicates the ideal position. The real velocity of the homogeneous medium is $V = 1/s = 4500$ m/s, and the reference velocity for each panel is $V_0 = 1/c = 1500$ m/s (upper left), 2250 m/s (lower left), 3000 m/s (lower right), and 3750 m/s (upper right), respectively. The grid interval used in migration is 10 m. The dominant frequency of the Ricker wavelet is 30 Hz.
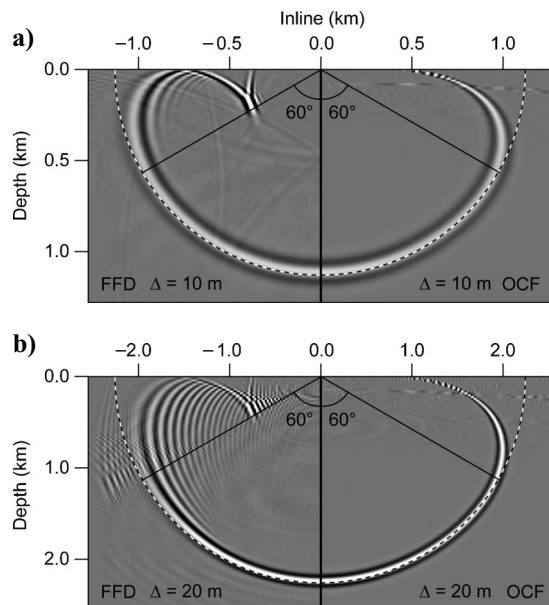

Figure 5. Vertical slices of 3D impulse responses obtained by the FFD method (left part of each panel) and the OCF method (right part of each panel). The dashed semicircle indicates the ideal position. A homogeneous medium with $V = 1/s = 4500$ m/s and $V_0 = 1/c = 1500$ m/s was used (i.e., $p = 1/3$). The dominant frequency of the Ricker wavelet is 30 Hz. The time delay of the Ricker wavelet is (a) 0.25 and (b) 0.5 s. The grid interval is (a) 10 and (b) 20 m.
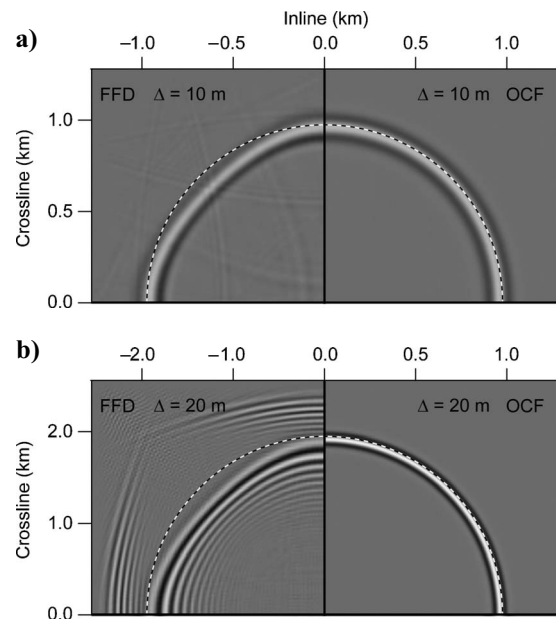

Figure 6. Depth slices of 3D impulse responses obtained by the FFD method (left part of each panel) and the OCF method (right part of each panel). This slice corresponds to the dip angle of 60° at 560 m depth in Figure 5. The dashed semicircle indicates the ideal position. A homogeneous medium with $V = 1/s = 4500$ m/s and $V_0 = 1/c = 1500$ m/s was used (i.e., $p = 1/3$). The dominant frequency of the Ricker wavelet is 30 Hz. The time delay of the Ricker wavelet is (a) 0.25 and (b) 0.5 s. The grid interval used in migration is (a) 10 and (b) 20 m.

band of the tapered function for the absorbing boundary condition has 15 samples on each side of the 2D wavefield. No wavenumber filter is used during the wavefield extrapolation.

Figure 7 shows the vertical and horizontal slices of the salt model, Figure 8 shows the corresponding vertical slices of imaged data, and Figure 9 shows the corresponding depth slices. In Figures 8 and 9, slices are obtained by the two-way splitting FFD method, the OCF method, and the GSP2 method, respectively. At first glance, it seems that most of the structures are well imaged. However, there are some apparent differences between the image results obtained by these three methods in the areas indicated by white arrows. The results obtained by the GSP2 method have more clear background but lower accuracy, especially for steep dips, when compared with the FFD method. The results obtained by the OCF method not only have more clear background but also have high accuracy for steep dips.

For detailed comparison, images within the rectangular areas in Figure 8 are shown in Figure 10. The steep dips obtained by the OCF method are much sharper than those obtained by the two-way splitting FFD method; in addition, the results have fewer numerical artifacts in the background or in the salt dome. Therefore, we see that the OCF method gives the best images among all methods listed.

These three methods have similar computational cost under the same hardware and software conditions, but both of the second-order Fourier methods are slightly slower than the FFD method. The FFD method runs 1217 s, the OCF method runs 1366 s, and the GSP2 method runs 1351 s.

DISCUSSION

The proposed scheme can be extended to higher orders, but the derivations are a little complex. We show the fourth-order propagator in Appendix D, and our theoretical analysis confirms that the fourth-order propagator has only slight improvement over the second-order propagator. The maximum dip angle of the fourth-order propagator under a relative error of 1% is about 65°, which is approximately 10° higher than that of the second-order propagator. However, six 2D Fourier transforms are required for each step of the 3D wavefield extrapolation; thus, the computing cost is about triple that of the SSF method. In contrast, only four 2D Fourier transforms are required for the second-order propagator; thus, the computing cost is twice that of the SSF method. Therefore, we suggest only the second-order OCF method in the text after compromising between accuracy and computational efficiency.

Figure 8. Vertical slices of 3D images obtained by the (a) FFD, (b) OCF, and (c) GSP2 methods. Note the vertical slices of migration results corresponding to Figure 7a.
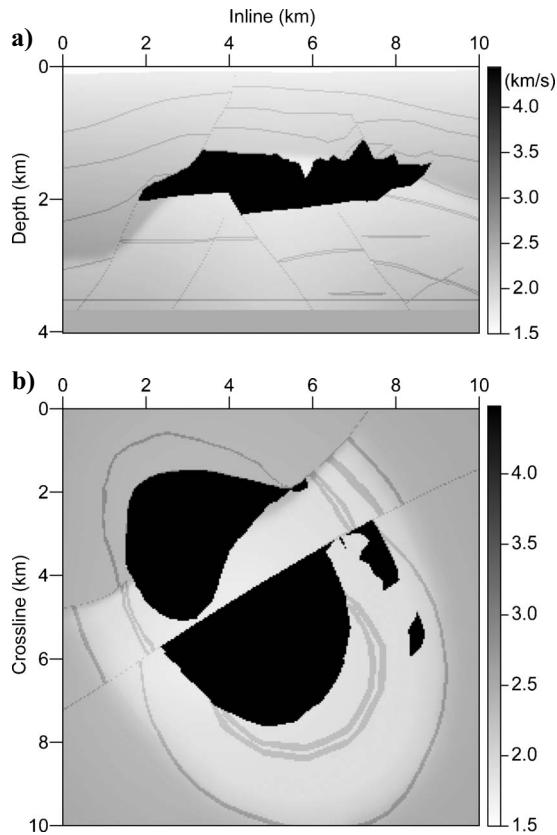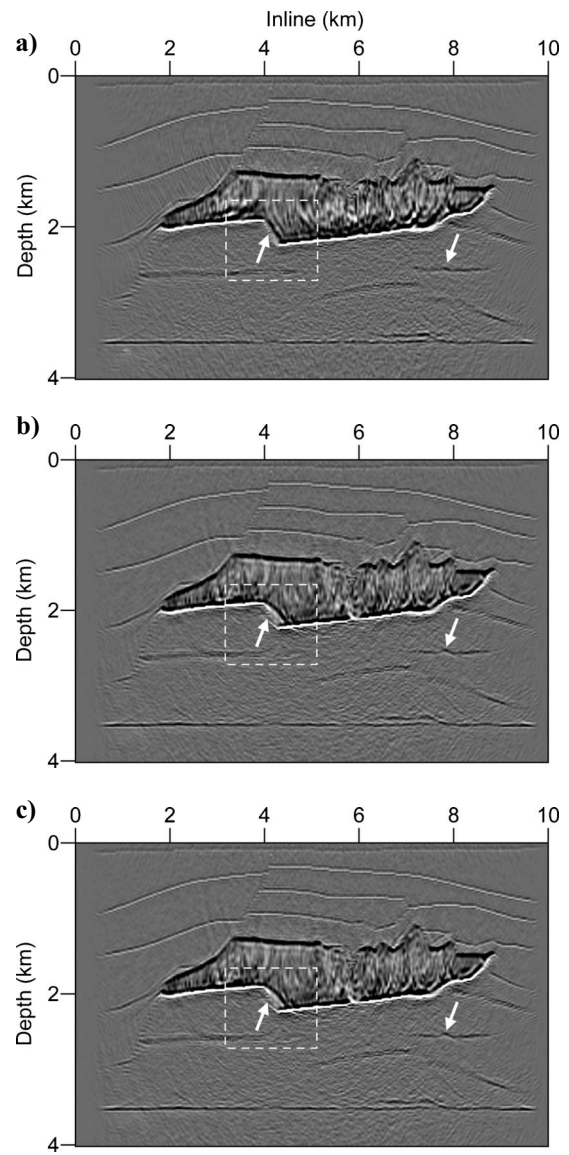

Figure 7. Slices of the 3D SEG/EAGE salt model: (a) vertical profile along the inline direction at a crossline position of 5000 m; (b) depth slice at 2010 m.

In prestack migration, the paths connecting the reflectors to the sources and receivers are usually at wide angles, especially for large-offset data. Thus, the wide-angle propagator is much more essential. Prestack migration, e.g., shot-profile migration, contains two similar parts: one is to propagate the source function and the other is to back extrapolate the recorded data. The one-way propagator is the core of each part. Although only the zero-offset migration is shown in this paper, it is easy to apply our propagator to prestack migration.

CONCLUSIONS

Accuracy of the approximated one-way propagator is a major factor that impacts the image results of 3D wave-equation migration. We have presented a Fourier propagator using truncated Chebyshev polynomials and a globally optimized scheme. We first use the Chebyshev truncation to reduce the phase error caused by the Taylor expansion of the square-root operator. Then we apply the Chebyshev truncation to reduce the phase error caused by the power series expansion of fractional-exponential functions. Finally, we use the globally optimized scheme to reduce the phase error further. The accurate dip angle of the OCF propagator is always around 60° for various velocity contrasts, comparable to that of the FFD propagator. This method allows us to accurately handle wide-angle wave propagations in complex media by only using Fourier transforms.

The OCF method is greatly encouraging for three reasons. First, the lower-order Fourier methods have difficulties in handling velocity contrasts, and their accurate dip angles hardly exceed that of the FFD method even for moderate velocity contrasts. Using the proposed method, we can now image steep dips for arbitrary (including weak, moderate, and strong) velocity contrasts as does the FFD method. Second, the proposed method is a pure Fourier method; thus, it has almost no numerical dispersions for coarse grids and high-frequency components, which are essential for high-resolution imaging. In addition, it has no splitting error for 3D implementation; thus, it can be extended accurately from two to three dimensions without difficulty. Finally, the computational cost of the proposed method mainly lies on the Fourier transforms; thus, it has more potential to be accelerated than the finite-difference method when a much faster Fourier transform algorithm arises. Therefore, our one-way propagator is better than the traditional FFD method in terms of maximum dip angle, numerical dispersion, splitting error, and computational cost.
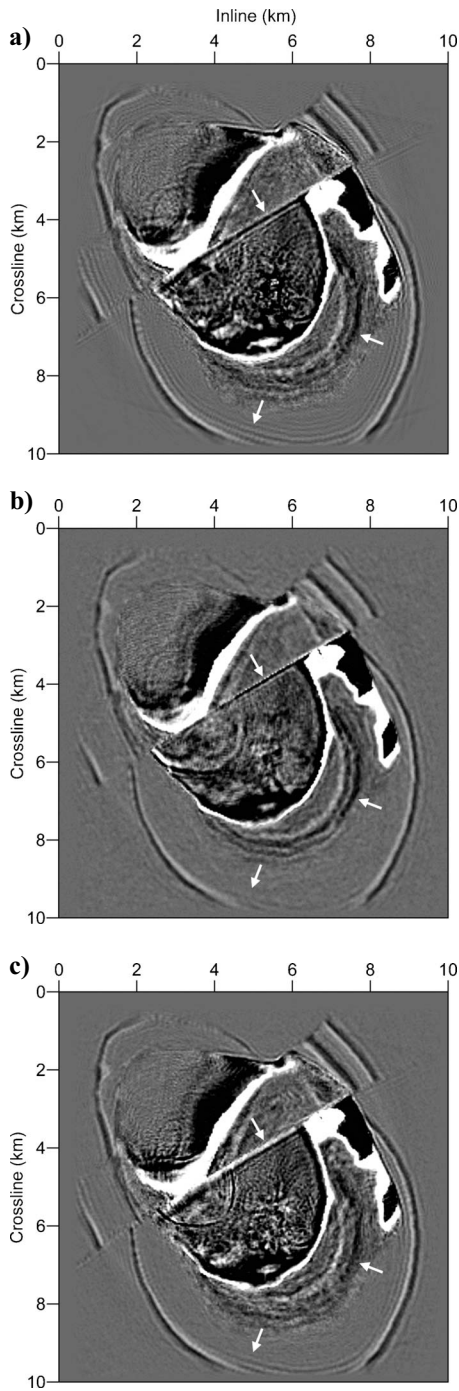
Figure 9. Depth slices of 3D images obtained by the (a) FFD, (b) OCF, and (c) GSP2 methods. Note the depth slices of migration results corresponding to Figure 7b.
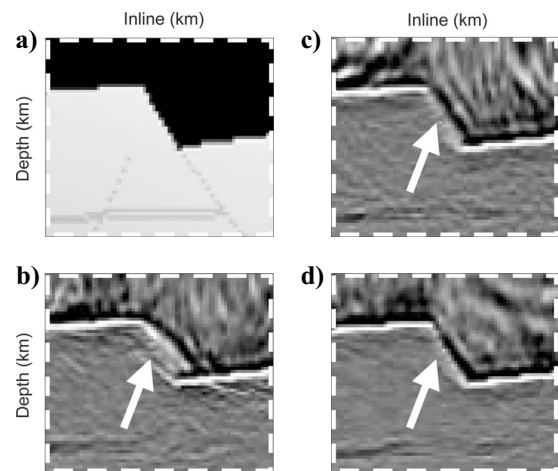

Figure 10. Comparison of the local details within the rectangular areas in Figure 8: (a) velocity model; (b) obtained by the GSP2 method; (c) obtained by the FFD method; (d) obtained by the OCF method.

APPENDIX A

BRIEF REVIEW OF CHEBYSHEV POLYNOMIALS

Chebyshev polynomials $T_n(\lambda)$ have n zeros and $n + 1$ uniformly distributed peaks whose maximum amplitude is 1 and minimum amplitude is -1, and the maximum error is minimal among various polynomials. In other words, the Chebyshev polynomials provide an approximation that is close to the polynomial of best approximation to a continuous function under the maximum norm.

For $|\lambda| \leq 1$, the Chebyshev polynomials of the first kind are defined by

$$T_n(\lambda) = \cos(n \cos^{-1} \lambda). \qquad \text{(A-1)}$$

From the recurrence relation

$$T_{n+1}(\lambda) = 2\lambda T_n(\lambda) - T_{n-1}(\lambda) \quad (n \geq 1), \qquad \text{(A-2)}$$

the first few Chebyshev polynomials are

$$T_0(\lambda) = 1,$$
$$T_1(\lambda) = \lambda,$$
$$T_2(\lambda) = 2\lambda^2 - 1,$$
$$T_3(\lambda) = 4\lambda^3 - 3\lambda,$$
$$T_4(\lambda) = 8\lambda^4 - 8\lambda^2 + 1,$$
$$T_5(\lambda) = 16\lambda^5 - 20\lambda^3 + 5\lambda,$$
$$\dots. \qquad \text{(A-3)}$$

Applying relations

$$1 = T_0,$$
$$\lambda = T_1,$$
$$\lambda^2 = \frac{1}{2}(T_0 + T_2),$$
$$\lambda^3 = \frac{1}{4}(3T_1 + T_3),$$
$$\lambda^4 = \frac{1}{8}(3T_0 + 4T_2 + T_4),$$
$$\lambda^5 = \frac{1}{16}(10T_1 + 5T_3 + T_5),$$
$$\dots, \qquad \text{(A-4)}$$

we could rewrite the Nth-order polynomial

$$k_z \approx \sum_{n=0}^{N} a_n \lambda^n \qquad \text{(A-5)}$$

as a Chebyshev polynomial

$$k_z \approx \sum_{n=0}^{N} a_n' T_n(\lambda). \qquad \text{(A-6)}$$

Neglecting the last term $T_N(\lambda)$ will reduce the order of the polynomial but with minimal loss of accuracy.

APPENDIX B

MAPPING FROM GENERAL RANGE $[a,b]$ TO $[-1,1]$

For any given finite range $[a,b]$ of μ, we can map this range to the range $[-1,1]$ of λ using the linear transformation

$$\lambda = \frac{2\mu - (a + b)}{b - a}. \qquad \text{(B-1)}$$

The Nth-order Taylor expansion of the vertical wavenumber $k_z = \sqrt{\omega^2 s^2 - k_x^2}$ around the maximum reference slowness c reads

$$k_z \approx \sqrt{\omega^2 c^2 - k_x^2} + \sum_{n=1}^{N} \frac{1}{n!} \left. \frac{\partial^n k_z}{\partial s^n} \right|_c \Delta s^n, \qquad \text{(B-2)}$$

where $\Delta s = s - c = c(p - 1)$ is the slowness perturbation and $p = s/c$ is the refraction index. The variable $\Delta s = c(p - 1) \leq 0$ ranges over $[c(p_{\min} - 1), 0]$, where $p_{\min} = \min[s/c]$. Defining $P \equiv c(p_{\min} - 1)$, we can map $\Delta s \in [P, 0]$ to $\lambda \in [-1,1]$ using relation $\Delta s = 0.5(1 - \lambda)P$. Thus, the Nth-order Taylor expansion shown in equation B-2 can be rearranged as a polynomial of λ:

$$k_z \approx \sum_{n=0}^{N} a_n \lambda^n, \qquad \text{(B-3)}$$

where

$$a_n = (-1)^n \sum_{j=n}^{N} \frac{P^j}{2^j j!} \left. \frac{\partial^j k_z}{\partial s^j} \right|_c.$$

APPENDIX C

SECOND-ORDER PROPAGATOR USING TRUNCATED CHEBYSHEV POLYNOMIALS

If we truncate the Chebyshev polynomials to the second order T_2, we obtain

$$k_z \approx a_0 + \left(a_1 + \frac{3}{4}a_3 \right)\lambda + a_2\lambda^2, \qquad \text{(C-1)}$$

where

$$a_0 = \sqrt{\omega^2 c^2 - k_x^2} + \frac{P}{2} \left. \frac{\partial k_z}{\partial s} \right|_c + \frac{P^2}{8} \left. \frac{\partial^2 k_z}{\partial s^2} \right|_c + \frac{P^3}{48} \left. \frac{\partial^3 k_z}{\partial s^3} \right|_c,$$

$$a_1 = -\frac{P}{2} \left. \frac{\partial k_z}{\partial s} \right|_c - \frac{P^2}{4} \left. \frac{\partial^2 k_z}{\partial s^2} \right|_c - \frac{P^3}{16} \left. \frac{\partial^3 k_z}{\partial s^3} \right|_c,$$

$$a_2 = \frac{P^2}{8} \left. \frac{\partial^2 k_z}{\partial s^2} \right|_c + \frac{P^3}{16} \left. \frac{\partial^3 k_z}{\partial s^3} \right|_c,$$

$$a_3 = -\frac{P^3}{48} \left. \frac{\partial^3 k_z}{\partial s^3} \right|_c.$$

Now mapping λ backward to Δs, we obtain

$$k_z \approx a_0 + a_1 + a_2 + \frac{3}{4}a_3 - \frac{4a_1 + 8a_2 + 3a_3}{2P}\Delta s + \frac{4a_2}{P^2}\Delta s^2. \tag{C-2}$$

According to the Chebyshev polynomials and the power series expansion

$$(1-x)^{-m} \approx 1 + mx + \frac{m(m+1)}{2!}x^2$$
$$+ \frac{m(m+1)(m+2)}{3!}x^3 \cdots, \quad m > 0, |x| < 1, \tag{C-3}$$

we approximate the fractional exponential functions $\partial^n k_z / \partial s^n|_c$ in $a_0 \sim a_3$ to the second order as

$$\left. \frac{\partial k_z}{\partial s} \right|_c \approx \omega + \frac{47\omega}{64}\frac{k_x^2}{\omega^2 c^2} + \frac{3\omega}{8}\frac{k_x^4}{\omega^4 c^4},$$

$$\left. \frac{\partial^2 k_z}{\partial s^2} \right|_c \approx -\frac{k_x^2}{\omega c^3}\left(1 + \frac{3}{2}\frac{k_x^2}{\omega^2 c^2}\right),$$

$$\left. \frac{\partial^3 k_z}{\partial s^3} \right|_c \approx \frac{3k_x^2}{\omega c^4}\left(1 + \frac{5}{2}\frac{k_x^2}{\omega^2 c^2}\right). \tag{C-4}$$

The truncated Chebyshev polynomials shown in equation C-2 become

$$k_z \approx \sqrt{\omega^2 c^2 - k_x^2} + \frac{P^3 k_x^2}{64\omega c^4}\left(1 + \frac{5}{2}\frac{k_x^2}{\omega^2 c^2}\right) + \left[\omega + \frac{47\omega}{64}\frac{k_x^2}{\omega^2 c^2}\right.$$
$$+ \frac{3\omega}{8}\frac{k_x^4}{\omega^4 c^4} - \frac{9P^2 k_x^2}{32\omega c^4}\left(1 + \frac{5}{2}\frac{k_x^2}{\omega^2 c^2}\right)\bigg]\Delta s + \left[-\frac{k_x^2}{2\omega c^3}\left(1\right.\right.$$
$$+ \frac{3}{2}\frac{k_x^2}{\omega^2 c^2}\bigg) + \frac{3P k_x^2}{4\omega c^4}\left(1 + \frac{5}{2}\frac{k_x^2}{\omega^2 c^2}\right)\bigg]\Delta s^2, \tag{C-5}$$

which can be rearranged into

$$k_z \approx \sqrt{\omega^2 c^2 - k_x^2} + \omega\Delta s + b_1\frac{\omega k_x^2}{\omega^2 c^2} + b_2\frac{\omega k_x^4}{\omega^4 c^4}, \tag{C-6}$$

where

$$b_1 = \frac{47\Delta s}{64} - \frac{1}{2c}\Delta s^2 + P_0,$$

$$b_2 = \frac{3\Delta s}{8} - \frac{3}{4c}\Delta s^2 + \frac{5}{2}P_0, \tag{C-7}$$

with

$$P_0 = \frac{P^3}{64c^2} - \frac{9P^2}{32c^2}\Delta s + \frac{3P}{4c^2}\Delta s^2.$$

APPENDIX D

FOURTH-ORDER PROPAGATOR USING TRUNCATED CHEBYSHEV POLYNOMIALS

Applying the fifth-order Taylor expansion on the vertical wavenumber k_z around the maximum reference slowness $c = 1/\min[V(x)]$ yields

$$k_z \approx \sqrt{\omega^2 c^2 - k_x^2} + \sum_{n=1}^{5} \frac{1}{n!} \left. \frac{\partial^n k_z}{\partial s^n} \right|_c \Delta s^n, \tag{D-1}$$

where

$$\left. \frac{\partial k_z}{\partial s} \right|_c = \omega^2 c(\omega^2 c^2 - k_x^2)^{-1/2},$$

$$\left. \frac{\partial^2 k_z}{\partial s^2} \right|_c = -\omega^2 k_x^2(\omega^2 c^2 - k_x^2)^{-3/2},$$

$$\left. \frac{\partial^3 k_z}{\partial s^3} \right|_c = 3\omega^4 k_x^2 c(\omega^2 c^2 - k_x^2)^{-5/2},$$

$$\left. \frac{\partial^4 k_z}{\partial s^4} \right|_c = -3\omega^4 k_x^2(4\omega^2 c^2 + k_x^2)(\omega^2 c^2 - k_x^2)^{-7/2},$$

$$\left. \frac{\partial^5 k_z}{\partial s^5} \right|_c = 15\omega^6 k_x^2 c(4\omega^2 c^2 + 3k_x^2)(\omega^2 c^2 - k_x^2)^{-9/2}. \tag{D-2}$$

Using relation $\Delta s = 0.5(1 - \lambda)P$, we can rewrite equation D-1 with the argument of λ as

$$k_z \approx a_0 + a_1\lambda + a_2\lambda^2 + a_3\lambda^3 + a_4\lambda^4 + a_5\lambda^5. \tag{D-3}$$

If we truncate the Chebyshev polynomials to the fourth order T_4, we obtain

$$k_z \approx a_0 + \left(a_1 - \frac{5}{16}a_5\right)\lambda + a_2\lambda^2 + \left(a_3 + \frac{5}{4}a_5\right)\lambda^3 + a_4\lambda^4, \tag{D-4}$$

where

$$a_0 = \sqrt{\omega^2 c^2 - k_x^2} + \frac{P}{2}\left.\frac{\partial k_z}{\partial s}\right|_c + \frac{P^2}{8}\left.\frac{\partial^2 k_z}{\partial s^2}\right|_c + \frac{P^3}{48}\left.\frac{\partial^3 k_z}{\partial s^3}\right|_c$$
$$+ \frac{P^4}{384}\left.\frac{\partial^4 k_z}{\partial s^4}\right|_c + \frac{P^5}{3840}\left.\frac{\partial^5 k_z}{\partial s^5}\right|_c,$$

$$a_1 = -\frac{P}{2}\left.\frac{\partial k_z}{\partial s}\right|_c - \frac{P^2}{4}\left.\frac{\partial^2 k_z}{\partial s^2}\right|_c - \frac{P^3}{16}\left.\frac{\partial^3 k_z}{\partial s^3}\right|_c$$
$$- \frac{P^4}{96}\left.\frac{\partial^4 k_z}{\partial s^4}\right|_c - \frac{P^5}{768}\left.\frac{\partial^5 k_z}{\partial s^5}\right|_c,$$

$$a_2 = \frac{P^2}{8} \left.\frac{\partial^2 k_z}{\partial s^2}\right|_c + \frac{P^3}{16} \left.\frac{\partial^3 k_z}{\partial s^3}\right|_c + \frac{P^4}{64} \left.\frac{\partial^4 k_z}{\partial s^4}\right|_c$$

$$+ \frac{P^5}{384} \left.\frac{\partial^5 k_z}{\partial s^5}\right|_c,$$

$$a_3 = -\frac{P^3}{48} \left.\frac{\partial^3 k_z}{\partial s^3}\right|_c - \frac{P^4}{96} \left.\frac{\partial^4 k_z}{\partial s^4}\right|_c - \frac{P^5}{384} \left.\frac{\partial^5 k_z}{\partial s^5}\right|_c,$$

$$a_4 = \frac{P^4}{384} \left.\frac{\partial^4 k_z}{\partial s^4}\right|_c + \frac{P^5}{768} \left.\frac{\partial^5 k_z}{\partial s^5}\right|_c,$$

$$a_5 = -\frac{P^5}{3840} \left.\frac{\partial^5 k_z}{\partial s^5}\right|_c.$$

Mapping λ backward to Δs, we obtain

$$k_z \approx a_0 + a_1 + a_2 + a_3 + a_4 + \frac{15}{16}a_5 - \left(2a_1 + 4a_2 + 6a_3\right.$$

$$\left.+ 8a_4 + \frac{55}{8}a_5\right)\frac{\Delta s}{P} + (4a_2 + 12a_3 + 24a_4 + 15a_5)\frac{\Delta s^2}{P^2}$$

$$- (8a_3 + 32a_4 + 10a_5)\frac{\Delta s^3}{P^3} + 16a_4\frac{\Delta s^4}{P^4} \quad\quad \text{(D-5)}$$

and

$$k_z \approx \sqrt{\omega^2 c^2 - k_x^2} + \sum_{n=1}^{4} \frac{1}{n!} \left.\frac{\partial^n k_z}{\partial s^n}\right|_c \Delta s^n + \alpha \left.\frac{\partial^5 k_z}{\partial s^5}\right|_c P^5,$$

$$\text{(D-6)}$$

where

$$\alpha \equiv \frac{1}{61440} - \frac{5}{6144}\frac{\Delta s}{P} + \frac{5}{768}\frac{\Delta s^2}{P^2} - \frac{7}{384}\frac{\Delta s^3}{P^4} + \frac{1}{48}\frac{\Delta s^4}{P^4}.$$

$$\text{(D-7)}$$

Approximating the fractional-exponential functions $\left.\partial^n k_z / \partial s^n\right|_c$ in $a_0 \sim a_5$ to the fifth order of variable k_x^2 first by the power series expansion and then by truncated Chebyshev polynomials, we obtain

$$\left.\frac{\partial k_z}{\partial s}\right|_c \approx \omega\left(1 + \frac{1733}{4096}\frac{k_x^2}{\omega^2 c^2} + \frac{3}{8}\frac{k_x^4}{\omega^4 c^4} + \frac{635}{1024}\frac{k_x^6}{\omega^6 c^6}\right.$$

$$\left.+ \frac{35}{128}\frac{k_x^8}{\omega^8 c^8}\right),$$

$$\left.\frac{\partial^2 k_z}{\partial s^2}\right|_c \approx -\frac{\omega}{c}\left(\frac{709}{1024}\frac{k_x^2}{\omega^2 c^2} + \frac{3}{2}\frac{k_x^4}{\omega^4 c^4} + \frac{555}{128}\frac{k_x^6}{\omega^6 c^6}\right.$$

$$\left.+ \frac{35}{16}\frac{k_x^8}{\omega^8 c^8}\right),$$

$$\left.\frac{\partial^3 k_z}{\partial s^3}\right|_c \approx \frac{3\omega}{c^2}\left(-\frac{131}{1024}\frac{k_x^2}{\omega^2 c^2} + \frac{5}{2}\frac{k_x^4}{\omega^4 c^4} + \frac{1715}{128}\frac{k_x^6}{\omega^6 c^6}\right.$$

$$\left.+ \frac{105}{16}\frac{k_x^8}{\omega^8 c^8}\right),$$

$$\left.\frac{\partial^4 k_z}{\partial s^4}\right|_c \approx -\frac{3\omega}{c^3}\left(4\frac{k_x^2}{\omega^2 c^2} + \frac{933}{16}\frac{k_x^4}{\omega^4 c^4} + \frac{2933}{64}\frac{k_x^6}{\omega^6 c^6}\right.$$

$$\left.+ \frac{63}{8}\frac{k_x^8}{\omega^8 c^8}\right),$$

$$\left.\frac{\partial^5 k_z}{\partial s^5}\right|_c \approx \frac{15\omega}{c^4}\left(4\frac{k_x^2}{\omega^2 c^2} + \frac{1623}{16}\frac{k_x^4}{\omega^4 c^4} + \frac{7893}{64}\frac{k_x^6}{\omega^6 c^6}\right.$$

$$\left.+ \frac{297}{8}\frac{k_x^8}{\omega^8 c^8}\right). \quad\quad \text{(D-8)}$$

Thus, the truncated Chebyshev polynomials of vertical wavenumber k_z shown in equation D-5 become

$$k_z \approx \sqrt{\omega^2 c^2 - k_x^2} + \omega\Delta s + \sum_{n=1}^{4} b_n\left(\frac{k_x^2}{\omega^2 c^2}\right)^n, \quad \text{(D-9)}$$

where

$$b_1 = \frac{1733\omega}{4096}\Delta s - \frac{709\omega}{2048c}\Delta s^2 - \frac{131\omega}{2048c^2}\Delta s^3 - \frac{\omega}{2c^3}\Delta s^4$$

$$+ \frac{60\omega}{c^4}\alpha P^5,$$

$$b_2 = \frac{3\omega}{8}\Delta s - \frac{3\omega}{4c}\Delta s^2 + \frac{5\omega}{4c^2}\Delta s^3 - \frac{933\omega}{128c^3}\Delta s^4$$

$$+ \frac{24345\omega}{16c^4}\alpha P^5,$$

$$b_3 = \frac{635\omega}{1024}\Delta s - \frac{555\omega}{256c}\Delta s^2 + \frac{1715\omega}{256c^2}\Delta s^3 - \frac{2933\omega}{512c^3}\Delta s^4$$

$$+ \frac{118395\omega}{64c^4}\alpha P^5,$$

$$b_4 = \frac{35\omega}{128}\Delta s - \frac{35\omega}{32c}\Delta s^2 + \frac{105\omega}{32c^2}\Delta s^3 - \frac{63\omega}{64c^3}\Delta s^4$$

$$+ \frac{4455\omega}{8c^4}\alpha P^5. \quad\quad \text{(D-10)}$$

For the convenience of optimization, we rewrite spatial variables $b_1 \sim b_4$ as

$$b_1 = f_1\left(\frac{1733\omega}{4096}\Delta s - \frac{709\omega}{2048c}\Delta s^2 - \frac{131\omega}{2048c^2}\Delta s^3 - \frac{\omega}{2c^3}\Delta s^4\right.$$

$$\left.+ \frac{60\omega}{c^4}\alpha P_1\right),$$

$$b_2 = f_2\left(\frac{3\omega}{8}\Delta s - \frac{3\omega}{4c}\Delta s^2 + \frac{5\omega}{4c^2}\Delta s^3 - \frac{933\omega}{128c^3}\Delta s^4\right.$$

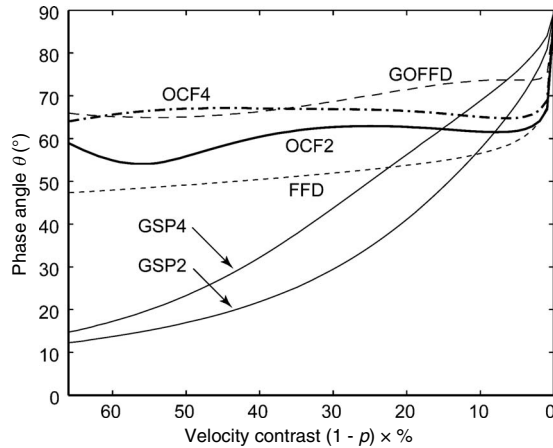$$\left.+ \frac{24345\omega}{16c^4}\alpha P_1\right),$$

Figure D-1. Maximum dip angles versus velocity contrasts under a relative error of 1%. This figure is similar to Figure 2 except that the fourth-order OCF method is added. The short dashed line denotes the FFD method; the long dashed line denotes the GOFFD method; the bold solid line denotes the second-order optimized Chebyshev Fourier method used in the text (OCF2); the bold dashed-dotted line denotes the fourth-order optimized Chebyshev Fourier method listed in Appendix D (OCF4); and the solid lines indicated by arrows denote the second and fourth orders of the generalized-screen methods, i.e., GSP2 and GSP4, respectively.

$$b_3 = f_3 \left(\frac{635\omega}{1024} \Delta s - \frac{555\omega}{256c} \Delta s^2 + \frac{1715\omega}{256c^2} \Delta s^3 - \frac{2933\omega}{512c^3} \Delta s^4 \right.$$

$$\left. + \frac{118395\omega}{64c^4} \alpha P_1 \right),$$

$$b_4 = f_4 \left(\frac{35\omega}{128} \Delta s - \frac{35\omega}{32c} \Delta s^2 + \frac{105\omega}{32c^2} \Delta s^3 - \frac{63\omega}{64c^3} \Delta s^4 \right.$$

$$\left. + \frac{4455\omega}{8c^4} \alpha P_1 \right), \tag{D-11}$$

with $P_1 = f_5(p-1)^4/p$, where $f_1 \sim f_5$ are constant coefficients ready to be optimized over $[0, 2]$.

Over the range of $p \in [1/3, 1]$ under the relative error of 1%, the optimized coefficients obtained are

$$f_1 = 1.1085748,$$

$$f_2 = 0.5547990,$$

$$f_3 = 1.3589634,$$

$$f_4 = 1.5193214,$$

$$f_5 = 1.5174208. \tag{D-12}$$

Figure D-1 shows the maximum dip angles versus the lateral velocity contrasts. The maximum dip angle of the fourth-order OCF method is higher than that of the second-order at about 10°.

REFERENCES

Aminzadeh, F., N. Burkhard, J. Long, T. Kunz, and P. Duclos, 1996, Three dimensional SEG/EAGE models — An update: The Leading Edge, **15**, 131–134.
Baysal, E., D. D. Kosloff, and J. W. C. Sherwood, 1983, Reverse time migration: Geophysics, **48**, 1514–1524.
Biondi, B., 2002, Stable wide-angle Fourier finite-difference downward ex-

trapolation of 3D wavefields: Geophysics, **67**, 872–882.
Brown, D. L., 1983, Applications of operator separation in reflection seismology: Geophysics, **48**, 288–294.
Chen, J. B., and H. Liu, 2004, Optimization approximation with separable variables for the one-way operator: Geophysical Research Letters, **31**, L06613.
Cheng, N., C. H. Cheng, and M. N. Toksöz, 1996, Error analysis of phase screen method in 3-D: Geophysical Research Letters, **23**, 1841–1844.
Claerbout, J. F., 1985, Imaging the earth's interior: Blackwell Scientific Publications, Inc.
de Hoop, M. V., J. H. Le Rousseau, and R. S. Wu, 2000, Generalization of the phase-screen approximation for the scattering of acoustic waves: Wave Motion, **31**, 285–296.
Fu, L. Y., 2005, Broadband constant-coefficient propagators: Geophysical Prospecting, **53**, 299–310.
Gazdag, J., 1978, Wave equation migration with the phase-shift method: Geophysics, **43**, 1342–1351.
Gazdag, J., and P. Sguazzero, 1984, Migration of seismic data by phase shift plus interpolation: Geophysics, **49**, 124–131.
Huang, L. J., and M. C. Fehler, 1998, Accuracy analysis of the split-step Fourier propagator: Implications for seismic modeling and migration: Bulletin of the Seismological Society of America, **88**, 18–29.
——, 2000a, Globally optimized Fourier finite-difference migration method: 70th Annual International Meeting, SEG, Expanded Abstracts, 802–805.
——, 2000b, Quasi-Born Fourier migration: Geophysical Journal International, **140**, 521–534.
Huang, L.-J., M. C. Fehler, P. M. Roberts, and C. C. Burch, 1999a, Extended local Rytov Fourier migration method: Geophysics, **64**, 1535–1545.
Huang, L.-J., M. C. Fehler, and R.-S. Wu, 1999b, Extended local Born Fourier migration method: Geophysics, **64**, 1524–1534.
Kelamis, P. G., 1988, On the theory of Chebyshev polynomial in wave-equation migration: Geophysical Journal International, **94**, 421–426.
Kirkpatrick, S., C. D. Gelatt, and M. P. Vecchi, 1983, Optimization by simulated annealing: Science, **220**, 671–680.
Kosloff, D. D., and E. Baysal, 1983, Migration with the full acoustic wave equation: Geophysics, **48**, 677–687.
Le Rousseau, J. H., and M. V. de Hoop, 2001, Modeling and imaging with the scalar generalized-screen algorithms in isotropic media: Geophysics, **66**, 1551–1568.
Li, Z., 1991, Compensating finite-difference errors in 3D migration and modeling: Geophysics, **56**, 1650–1660.
Liu, L., and J. Zhang, 2006, 3D wavefield extrapolation with optimum split-step Fourier method: Geophysics, **71**, no. 3, T95–T108.
Loewenthal, D., and I. R. Mufti, 1983, Reversed time migration in spatial frequency domain: Geophysics, **46**, 627–635.
Mason, J. C., and D. C. Handscomb, 2003, Chebyshev polynomials: Chapman and Hall/CRC Press.
Ober, C. C., R. A. Oldfield, D. E. Womble, and C. C. Mosher, 1997, Seismic imaging on massively parallel computers: 67th Annual International Meeting, SEG, Expanded Abstracts, 1418–1421.
Ristow, D., and T. Rühl, 1994, Fourier finite-difference migration: Geophysics, **59**, 1882–1893.
Sen, S., and S. Anandakrishnan, 2003, Optimized steep dip Fourier finite-difference migration using Chebyshev polynomials and simulated annealing: Fall Meeting, American Geophysical Union, Abstracts, S51A-04.
Stoffa, P. L., J. T. Fokkema, R. M. de Luna Freire, and W. P. Kessinger, 1990, Split-step Fourier migration: Geophysics, **55**, 410–421.
Wang, Y., 2001, ADI plus interpolation: Accurate finite-difference solution to 3D paraxial wave equation: Geophysical Prospecting, **49**, 547–556.
Wu, R. S., 1994, Wide-angle elastic wave one-way propagation in heterogeneous media and an elastic wave complex-screen method: Journal of Geophysical Research, **99**, 751–766.
Xie, X. B., and R. S. Wu, 2001, Modeling elastic wave forward propagation and reflection using the complex screen method: Journal of the Acoustical Society of America, **109**, 2629–2635.
Zhang, G. Q., S. L. Zhang, Y. X. Wang, and C. Y. Liu, 1988, A new algorithm for finite-difference migration of steep dips: Geophysics, **53**, 167–175.
Zhang, J., and L. Liu, 2007, Optimum split-step Fourier 3D depth migration: Developments and practical aspects: Geophysics, **72**, no. 3, S167–S175.
Zhang, J. H., W. M. Wang, L. Y. Fu, and Z. X. Yao, 2008, 3D Fourier finite-difference migration by ADI plus interpolation: Geophysical Prospecting, **56**, 95–103.
Zhang, J. H., S. Q. Wang, and Z. X. Yao, 2009a, Accelerating 3D Fourier migration with graphics processing units: Geophysics, **74**, no. 6, WCA129–WCA139.
——, 2009b, Comparison between the Fourier finite-difference method and the generalized-screen method: Geophysical Prospecting, **57**, 355–365.
Zhu, S. W., J. H. Zhang, and Z. X. Yao, 2008, Globally optimized Fourier finite-difference operator using simulated annealing algorithm based on multi-parameter: Chinese Journal of Geophysics, **50**, 1844–1850 (in Chinese).